

Microneedle-Based Local Delivery of CCL22 and IL-2 Enriches T_{reg} Homing to the Skin Allograft and Enables Temporal Monitoring of Immunotherapy Efficacy

Núria Puigmal, Pere Dosta, Zhabiz Solhjou, Karim Yatim, Cynthia Ramírez, John Y. Choi, Juliano B. Alhaddad, Ana Paula Cosme, Jamil Azzi,* and Natalie Artzi*

Skin allografts only serve as temporary dressing for patients suffering major burns due to their high immunogenicity and rejection by the immune system, requiring systemic immunosuppressive therapies that lead to deleterious side effects. Microneedle arrays composed of hyaluronic acid (HA) and placed on skin allografts can locally deliver immunomodulators and simultaneously sample immune cells in interstitial fluid to monitor the response to the therapy. The cells can be retrieved from the microneedles for downstream analysis by degrading the HA using a reducing agent. Using an allogeneic skin transplantation model, it is shown that the microneedle-mediated local delivery of the chemokine CCL22 (to attract T_{regs}) and the cytokine IL-2 (to promote their expansion) increases the local immune suppression in the allograft. Moreover, immune cell population in the allograft correlates with that seen in the microneedles. The delivery and sampling functions of the microneedle arrays can help regulate the immune system locally, without inducing systemic immune suppression, and facilitate the monitoring of the response to the therapy following skin transplantation.

organ transplantation, dermal immune cells can detect danger signals and resolve inflammation. CD4⁺CD25⁺FOXP3⁺ regulatory T cells (T_{regs}) are a subtype of T cells that suppress other activated immune cells and control the body's response to self- and foreign-antigens, in order to prevent overactivated immune responses such as in the case of autoimmune disorders.^[2] T_{regs} account for one of the largest subsets of immune cells in the skin, promoting local immunological homeostasis and restoring normal function after a threat.^[3,4] The increased proportion of T_{regs} in skin-resident CD4⁺ T cell population compared to other organs (20% in skin vs 5% in peripheral blood) also suggests an integral role for immune regulation in a tissue-specific manner.^[5,6] Indeed, disruption in skin T_{reg} homeostasis—due to dysregulated T_{reg} number or function—triggers disorders such as psoriasis,^[7] alopecia areata,^[8,9] diffuse systemic sclero-

derma, atopic dermatitis, or cutaneous lupus erythematosus.^[3] Hence, pharmacologic T_{reg} augmentation and adoptive T_{reg} transfer have emerged as means to manage autoimmune disorders and skin transplantation.


Skin allograft transplantation (from a genetically different individual) is the first-line therapy for severe burn patients and victims of traumatic injuries when autograft transplantation

1. Introduction

The skin is a complex organ that has evolved to protect the host from external insults. An intricate network of immune cells residing in the skin is crucial for host defense, wound healing, as well as for maintaining tissue homeostasis.^[1] In the event of a challenge such as a burn, autoimmune disease, or foreign

N. Puigmal, Dr. P. Dosta, C. Ramírez, A. P. Cosme, Prof. N. Artzi
Institute for Medical Engineering and Science
Massachusetts Institute of Technology
Cambridge, MA 02139, USA
E-mail: nartzi@bwh.harvard.edu

N. Puigmal, Dr. P. Dosta, C. Ramírez, A. P. Cosme, Prof. J. Azzi,
Prof. N. Artzi
Department of Medicine
Division of Engineering in Medicine
Brigham and Women's Hospital
Harvard Medical School
65 Landsdowne Street, Cambridge, MA 02139, USA
E-mail: jazz@bwh.harvard.edu

 The ORCID identification number(s) for the author(s) of this article can be found under <https://doi.org/10.1002/adfm.202100128>.

DOI: 10.1002/adfm.202100128

N. Puigmal
Grup d'Enginyeria de Materials (GEMAT)
Institut Químic de Sarrià
Universitat Ramon Llull
Via Augusta 390, Barcelona 08017, Spain

Dr. Z. Solhjou, Dr. J. Y. Choi, Dr. J. B. Alhaddad, Prof. J. Azzi
Department of Medicine
Division of Renal Medicine
Brigham and Women's Hospital
Harvard Medical School
221 Longwood Avenue, Boston, MA 02115, USA

Dr. K. Yatim
Department of Medicine
Division of General Internal Medicine and Primary Care
Brigham and Women's Hospital
Harvard Medical School
221 Longwood Avenue, Boston, MA 02115, USA

(from self) is not viable, due to insufficient healthy tissue for excision, donor site morbidity, or poor tolerability to additional surgeries.^[10–12] However, skin rejection following skin allotransplantation—the most immunogenic of all known allografts—is inevitable,^[13] arising from the intense immunogenicity of transplanted allografts harboring immunogenic antigens presented to the recipient's immune system.^[2] The current gold-standard therapy for the management of skin rejection is systemic immunosuppression, which partially suppresses rejection, at the cost of increasing the risk of opportunistic infections and incidence of malignancy.^[14,15] Since T_{regs} mediate specific functions depending entirely upon their residing tissues,^[6] tissue-specific therapeutic approaches should be favored to maximize their efficacy. Hence, skin allograft provides a unique opportunity for direct and easy access to the tissue that we leveraged by transcutaneously delivering immunotherapy using a microneedle-based platform.

Adoptive T_{reg} transfer aiming to expand skin-resident T_{regs} within the skin allograft has shown potential in restoring immunological homeostasis at the site of alloimmunity.^[14,16–18] However, widespread translation of this therapy into clinical settings has been limited due to the premature clearance of T_{regs} from serum and their need for a favorable immune environment, including IL-2, to ensure their survival and phenotypic stability.^[19] Post-transplant immunosuppressive therapies are known to generate a hostile IL-2 depleted milieu for T_{regs} proliferation,^[20,21] but attempting to counteract the levels of IL-2 via systemic administration has been constrained by risks of infection,^[22] vascular leak syndrome,^[23] and the expansion of other proinflammatory cell counterparts such as natural killer (NK) cells.^[24] Previous studies have also shown an increase in T_{reg} proliferation and population size in the spleen in response to systemic IL-2 delivery, while its effect on allograft survival has been limited compared to its broad range of side effects.^[25,26] Recently, CCL22 has been proposed as a powerful candidate to mediate migration of T_{regs} to the site of inflammation and reestablish donor-specific tolerance in different transplant models including pancreatic islets allografts and vascularized allograft composites.^[27–30]

In parallel, prompt recognition of rejection episodes is as critical as their management, particularly at early stages.^[31,32] However, current strategies to monitor skin transplant failure rely on gross observation and skin biopsies, which in addition to being invasive and biased due to the limited area that is being analyzed, becomes apparent late in the process, when intervention can no longer be effective.

MN-based delivery allows precise tissue localization within the skin,^[33,34] enhancing the efficacy and tolerability of the therapy by directly exposing it to the intended molecular targets and reducing the off-target effects associated with systemic approaches. The non-invasive and pain-free nature of MNs facilitate high patient compliance, while minimizing the risk of infections.^[35] MNs have also been proposed as a non-invasive tool for skin interstitial fluid (ISF) sampling. ISF is an accessible source of biomarkers that can inform on tissue physiology by monitoring soluble biomarkers and cellular fractions and in turn report on patient physiological state.^[36,37] Previous attempts have mainly focused on the extraction of soluble biomarkers from ISF, designing MNs for in situ detection of

metabolites,^[36,38] or necessitating downstream processing that involved physical methods such as high-speed centrifugation^[39,40] or heat treatments^[41] to collect biomarkers in ISF. Hence, digestible platforms are needed in order to retrieve and analyze cells while preserving their viability.^[42] In the context of transplantation, we hypothesized that ISF retrieval using MNs could be potentially utilized as a mode of tissue surveillance to study the response to the therapy.

Here, we designed a MN platform that enable simultaneous therapy delivery and tissue cell sampling to enhance the immune tolerogenic environment and to monitor changes in the tissue inflammatory state. We hypothesized that the local delivery of CCL22 together with IL-2 will induce substantial recruitment and localized expansion of T_{regs} in skin allografts, tilting the effector-to- T_{reg} cell ratio in favor of immunological homeostasis at the site of alloimmunity. Thus, we have developed a MN platform derived from Hyaluronic Acid (HA) for non-invasive delivery of immunomodulators (IL-2 and CCL22) to recruit endogenous and adoptively transferred T_{regs} to restore the tolerogenic environment at the transplant site. The MN platform will enable simultaneous sampling of ISF to study the T_{reg} homing process into the allograft as a response to the therapy and the presence of proinflammatory biomarkers (**Figure 1A**). While delivery of immune therapies using MNs has been achieved for the treatment of various diseases,^[43–45] our approach aims to induce immunoregulation in the allograft microenvironment, rather than immunosuppression, to avoid the deleterious side effect on the regulatory arm of the immune system and to allow for the patient's own immune system to clear the disease. The mechanical properties of our hydrogel-based MNs were engineered to ensure skin transplant penetration, high swelling capacity, and cell retrieval for adequate monitoring of the response to the therapy. The MNs were engineered to enable on-demand degradation (in less than 5 min) to recover the migrated immune cells while maintaining their viability, as a non-invasive mode of evaluation of the allograft inflammatory state.

2. Results and Discussion

2.1. Design of a Highly Swellable Microneedle Platform With On-Demand Degradation

In this study, we aimed to develop HA-based MNs to deliver immunomodulators while enabling simultaneous sampling of the cellular fraction in the skin ISF. HA is a biocompatible, non-immunogenic, and FDA-approved linear polysaccharide,^[46] which has been extensively used in the past for MN fabrication.^[39–41,47] HA's natural ability to absorb a large volume of water makes it an ideal candidate for rapid ISF extraction. In addition, HA can function as a natural ligand of the ubiquitous CD44 receptor,^[48] providing a binding motif for the cells present in ISF. Here, we chemically modified the HA polymer backbone to allow the formation of a digestible HA hydrogel capable of extracting both cellular and soluble biomarkers that are present in ISF upon patch retrieval. HA was modified with cysteamine dihydrochloride molecule, harboring both a primary amine group (for hydrogel formation) and a disulfide

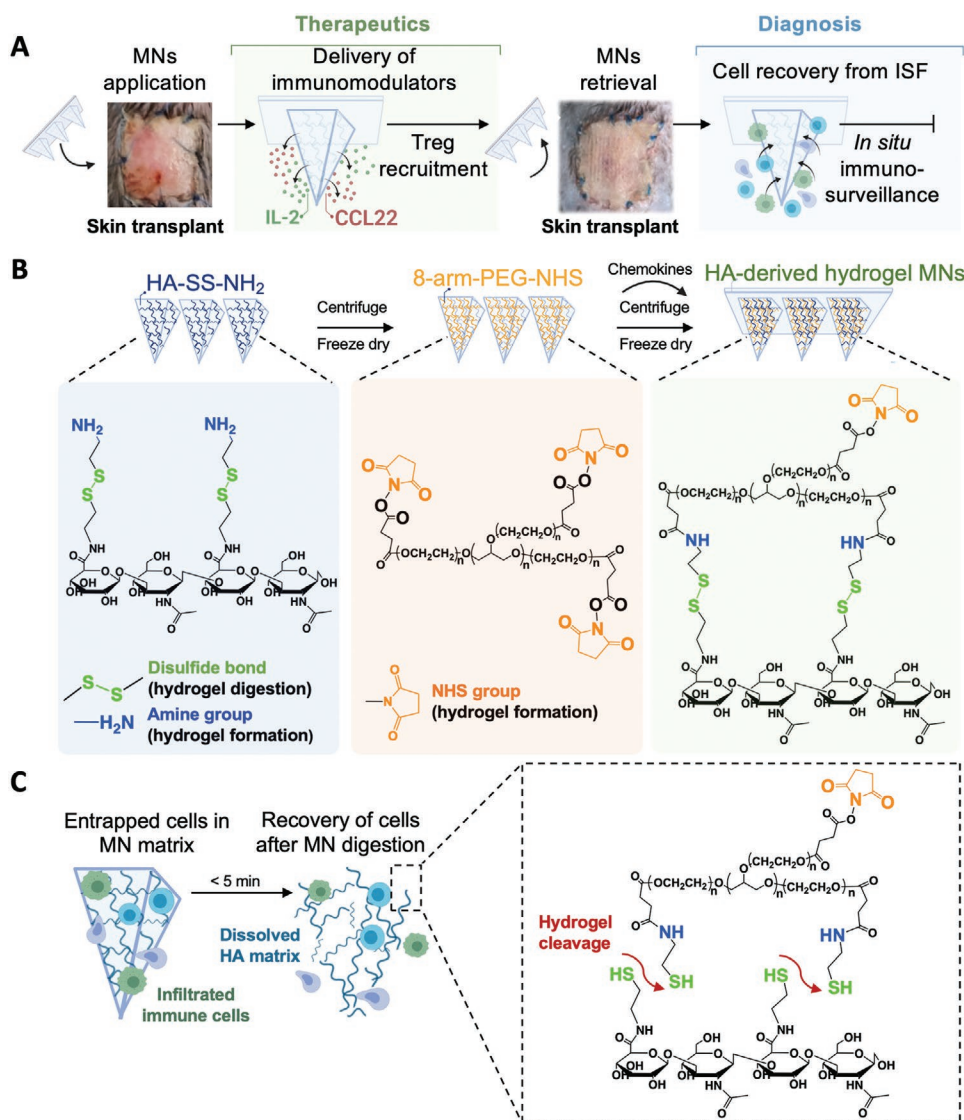


Figure 1. Design of an HA-based MN platform for non-invasive immunoregulation in skin transplants and immunosurveillance. A) Use of a novel HA-based MN platform that allows for: 1) delivery of immunomodulators for the recruitment of endogenous and adoptively transferred regulatory T cells, and 2) in situ cell sampling for monitoring the T_{reg} homing process. B) HA-based MN fabrication process. HA-based MNs were fabricated by casting an aqueous amine-modified HA (HA-SS-NH₂) solution into the PDMS mold by centrifugation and crosslinked using the NHS-terminated 8-arm PEG crosslinker. Chemokines were loaded and a PLGA back layer was added (top scheme). Chemical structure of the HA-SS-NH₂ crosslinked with NHS-terminated 8-arm PEG forming a digestible HA hydrogel through a disulfide bond (bottom scheme). C) Degradation of the MNs under reducing conditions enables facile recovery of retrieved cells. Disulfide bonds of the HA-based MNs are cleaved with 10 mM TCEP.

bond (for hydrogel degradation) (Figure 1B) whose structure was confirmed by ¹-NMR (Figures S1 and S2, Supporting Information). To form the HA-based hydrogel, HA primary amines were reacted with the 8-arm-PEG-NHS crosslinker containing a succinimidyl functional group (Figure 1B), allowing for spontaneous hydrogel formation without the use of external triggers. For MN fabrication (top scheme of Figure 1B), the HA-derived polymer was cast into a mold, centrifuged at high speed, and freeze-dried, creating a porous matrix that provided the scaffold to which subsequent components would be added. Next, the 8-arm-PEG-NHS crosslinker was added, followed

by the addition of an aqueous solution containing the immunomodulators IL-2 and CCL22. Finally, a backing-layer was deposited, serving as an anchor for MN administration and retrieval. The disulfide bond in the modified HA backbone allowed for on-demand cleavage to release the migrated cells following ISF sampling upon the addition of a reducing agent, tris (2-carboxyethyl) phosphine (TCEP—a water-soluble and non-toxic reducing agent widely used for biochemical applications).^[49] The addition of TCEP facilitated the collapse of the 3D structure of the hydrogel MNs and in turn, the release of the entrapped cells (Figure 1C).

2.2. Biophysical Characterization of the HA-Based MNs

To assess the HA-based MNs performance, the MNs swelling capacity, mechanical strength, and on-demand digestion were studied. We first investigated the influence of the crosslinking agent in determining the swelling capacity of the HA-NH₂-derived hydrogels as a function of weight gain over time. Three different crosslinking agents were screened, differing in their molecular weight: 40 kDa-8-arm-PEG-NHS (40 kDa-PEG), 10 kDa-8-arm-PEG-NHS (10 kDa-PEG), and their combination 70:30wt% of 40 kDa:10 kDa-PEG. Here, we opted for utilizing hydrogel disks rather than MNs that provided with about 30-fold increase in volume, to effectively screen for the best crosslinking agent. We found that the crosslinker type did not affect the initial swelling phase—an average swelling ratio of about 800% in less than an hour was observed for all hydrogels (Figure 2A). However, the crosslinker type had a marked influence on swelling at later time points with ratios of 1073% ± 58 and 1592% ± 36% for hydrogels derived from the 10 kDa-PEG and the 40 kDa-PEG, respectively. As expected, when the mixture of both crosslinkers was used, the swelling ratio was in between these values; 1191% ± 59%. Our results show that the choice of crosslinker—specifically, its molecular weight—allowed tailoring of the swelling capacity of the HA-derived hydrogels without the need of adding osmolytes such as sucrose or maltose to increase the osmotic pressure.^[40] Similar swelling phenomena were observed in stability studies where hydrogels

were incubated in physiologically-relevant conditions. The 40 kDa-PEG-derived-hydrogels dissolved after 48 h of incubation while the volume of the other hydrogels remained unchanged for extended periods of time (Table S1, Supporting Information). Next, the capacity of the MN patch to penetrate the skin was evaluated both ex vivo and in vivo using a murine model. Fine-tuning the crosslinking agent, both in terms of molecular weight and relative ratio, served as a powerful strategy to enhance the mechanical strength of our MNs, avoiding the use of solid core/shells and irreversible crosslinking strategies. The ability to form the entire needles from the hydrogels provides with higher volume for entrapment of ISF biomarkers, and thus permits better immune cell sampling and drug loading. Our ex vivo studies revealed that MNs containing 10 kDa-PEG (alone or when mixed with the 40 kDa-PEG) could efficiently disrupt the stratum corneum as confirmed by the accumulation of blue tissue-marking dye inside the micro conduits (Figure 2B), while those that were solely crosslinked with the PEG-40 kDa could not penetrate the viable skin. Similar results were observed in vivo (Figure 2C). Additionally, we confirmed via compression testing that the chemokine-loaded MNs did not modify the mechanical strength of the patch compared to empty needles nor their ability to penetrate the skin allografts (Figure S3, Supporting Information). Thus, we chose to proceed with the 70:30 40kDa:10kDa-PEG that provided both high swelling capacity and adequate mechanical properties to effectively pierce the mouse skin. We also characterized the ability

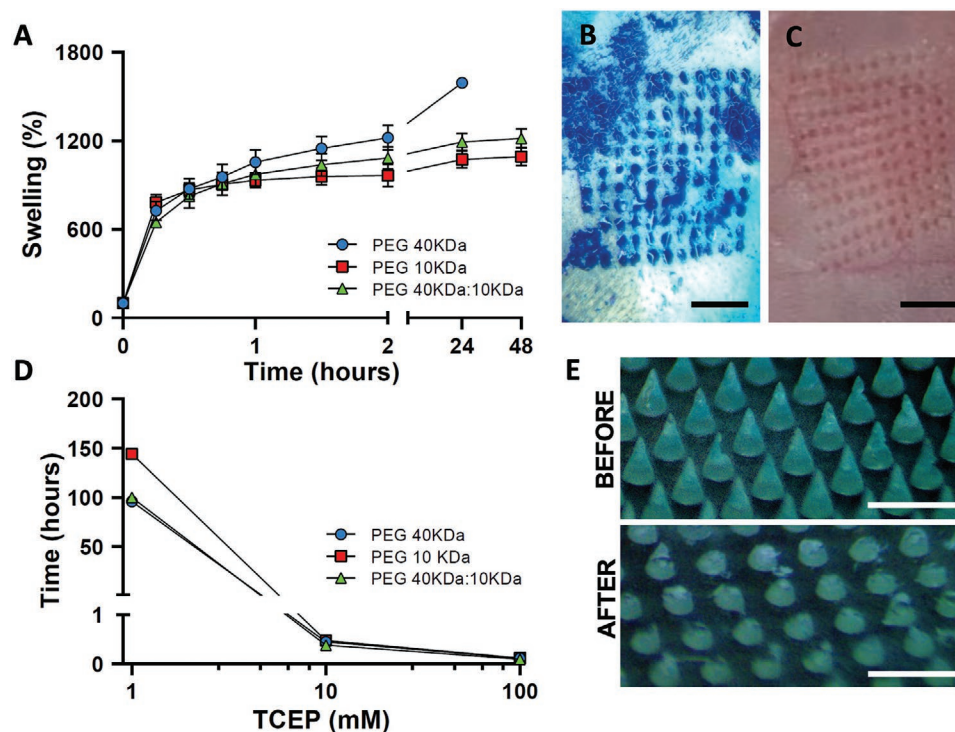


Figure 2. HA-modified hydrogel MNs present high swelling capacity, robust mechanical properties, and on-demand degradation. A) Swelling rate of the HA-based hydrogels composed of amine-modified HA polymer crosslinked with NHS-terminated 8-arm PEG crosslinkers differing in molecular weight. B) Stained skin graft following ex vivo HA-SS-NH₂-derived MN application confirms skin penetration. Scale bar = 2mm. C) Detail of mouse skin after in vivo administration of hydrogel MNs. Scale bar = 2mm. D) On-demand digestion of hydrogel disks using varying concentrations of the reducing agent, TCEP. E) Optical microscopy images of hydrogel-based MNs before (top) and after (bottom) digestion under reducing conditions. Scale bar = 500 μm. Data are represented as mean ± s.d. (n = 3).

to induce on-demand digestion of the MNs using TCEP, which we found was biocompatible and did not affect cell viability (Figure S4, Supporting Information), in agreement with our previous data.^[50] Studying the digestion kinetics of the HA-derived hydrogels confirmed a linear correlation between TCEP concentration and the time needed for full hydrogel digestion (Figure 2D). High concentrations of TCEP (>10 mM) ensured complete digestion in half an hour whereas hydrogel digestion was not accomplished, or was far too long, when TCEP concentration was lower than 1 mM. Considering these findings, our working concentration for further studies was 10 mM TCEP. We then studied the digestion kinetics of these hydrogels when in a MN form and we were able to confirm complete digestion of the MN array in less than 5 min (Figure 2E). The MNs high surface-area-to-volume ratio and low overall volume (~3 μ L) (compared to the hydrogel disks) facilitated the penetration of the reducing agent and accelerated their digestion.

2.3. HA-Based MNs for Simultaneous Drug Delivery and ISF Sampling

We initially studied the release kinetics of cytokines from the MNs using fluorescently labeled IL-2. Interestingly, no IL-2 was released (Figure 3A), which was attributed to the interaction between the IL-2-amine groups with unreacted free-NHS groups in the crosslinker, impeding its release. To validate this hypothesis, we blocked the interaction with the cytokines by treating the hydrogel with an end-capping agent—the amino acid glycine—whose amino-end groups would preferentially interact with the crosslinker's non-reacted NHS-terminal groups. Indeed, end-capping the hydrogel resulted in more than 80% of the cytokine being released within the first 30 min, which we then used in further studies. Next, the loading efficiency of IL-2 was investigated by fluorescence quantification, revealing a linear correlation between the loaded concentration and the retrieved one after digestion of the MN patch (Figure 3B), confirming the potential of our loading method to deliver biologically relevant dosages in the nanogram range.

Next, we examined the biological activity of chemokines when loaded into the MNs. Specifically, we studied the ability of CCL22 to mediate T_{reg} recruitment when delivered using the MN platform through a trans-well migration assay (Figure 3C). Briefly, varied concentrations of CCL22, either MN-doped or soluble, were incubated with $CD3^+$ T cells and the number of migrated T_{regs} was analyzed after 3 h of incubation by flow cytometry. Our results indicated a dose-dependent increase of T_{reg} migration for both soluble and MN-loaded CCL22 wells ($P = 0.02$ and 0.04 for soluble and MN respectively). Recruitment of T_{regs} by CCL22-containing MNs was comparable to that when adding soluble CCL22 at the same dose ($p = 0.9, 0.2, 0.2$ for 0, 10, and 100 ng mL^{-1}), suggesting that the chemokine functionality was not affected by the fabrication method. We also confirmed that the MN-loaded chemokines could be stored at 4 °C for up to one month without undergoing significant deterioration, as seen by ELISA (Figure S5, Supporting Information).

In parallel, we studied the diagnostic capacity of the platform and its ability to extract ISF in the absence of chemotactic

agents. Sampling of soluble biomarkers using MNs was investigated using a mimetic skin model.^[40,41] Briefly, agarose gels with comparable mechanical properties to that of the epidermis/ISF were covered with a stretched layer of parafilm that emulated the water-impermeable stratum corneum. Hydrogel-based MNs were applied to the skin model containing a model analyte, Rhodamine B (RhoB), which was recovered after digestion of the patches. Differences in RhoB concentration could be easily detected by gross observation as evidenced by the color change of the MN matrix after administration (Figure 3D, top). Quantification of the analyte absorbance confirmed a linear correlation between the concentration of RhoB in the skin-mimetic hydrogel and the concentration of the retrieved ISF when sampled using the hydrogel-based MNs (Figure 3D). Extraction of the cellular component of ISF was assessed by incubating the arrays of MNs in monocyte-like cell suspensions followed by their digestion to collect and measure the infiltrated cellular fraction. Arrays of solid, PLGA-based MNs were also incorporated to the analysis as controls to discern whether recovered cells were embedded within the hydrogel matrix or originated from non-specific interactions with the MN walls. Quantification of the digested suspension by flow cytometry depicted that cells were diffusing into the hydrogel MNs and remained inside the matrix (Figure 3E). As expected, the number of cells recovered from the solid arrays was practically negligible. Results also pointed at a correlation between the swelling ability of the hydrogel and cell infiltration. We found that a higher number of cells appeared to be infiltrated within MNs formulated with the 40 kDa-crosslinker compared to the other formulations.

2.4. Delivery of CCL22 and IL-2 to Skin Allografts via MNs Results in Increased T_{reg} Recruitment and Reduced Inflammation In Vivo

After exploring the ability of our MNs to rapidly release chemokines in vitro, we studied the MN local immunomodulatory function in vivo using a fully mismatched major histocompatibility complex (MHC) skin transplant model, which is a highly immunogenic model of rejection (Figure 4A). We synthesized MNs loaded with CCL22 and IL-2, at two different concentrations (100 ng CCL22+10 ng IL-2 or 100 ng CCL22+100 ng IL-2), with the rationale being for CCL22 to enhance the recruitment of T_{regs} , and for IL-2 to maintain T_{reg} homeostasis in vivo.^[20,21] We then grafted a 10 mm \times 15 mm skin patch recovered from BALB/cJ mouse onto the dorsal trunk of an immunodeficient recombination activation gene 1 knockout ($Rag^{-/-}$) mouse on C57BL/6 background, which lacks both T and B cells. Skin graft was dressed and left to heal for 5 days. On day 6 post-transplant, 7×10^6 magnetically isolated T lymphocytes were adoptively transferred to induce rejection in the allograft recipients as previously described by us.^[51] One day post adoptive transfer, MNs (100 ng CCL22+10 ng IL-2 or 100 ng CCL22+100 ng IL-2) were applied daily on the skin allograft for five consecutive days, with one group of mice receiving empty MNs as a control. Recipient mice were euthanized at day 7 post T_{reg} adoptive transfer and skin grafts harvested and studied by quantitative PCR to measure tissue T_{reg} infiltration and gene expression. We saw indentations

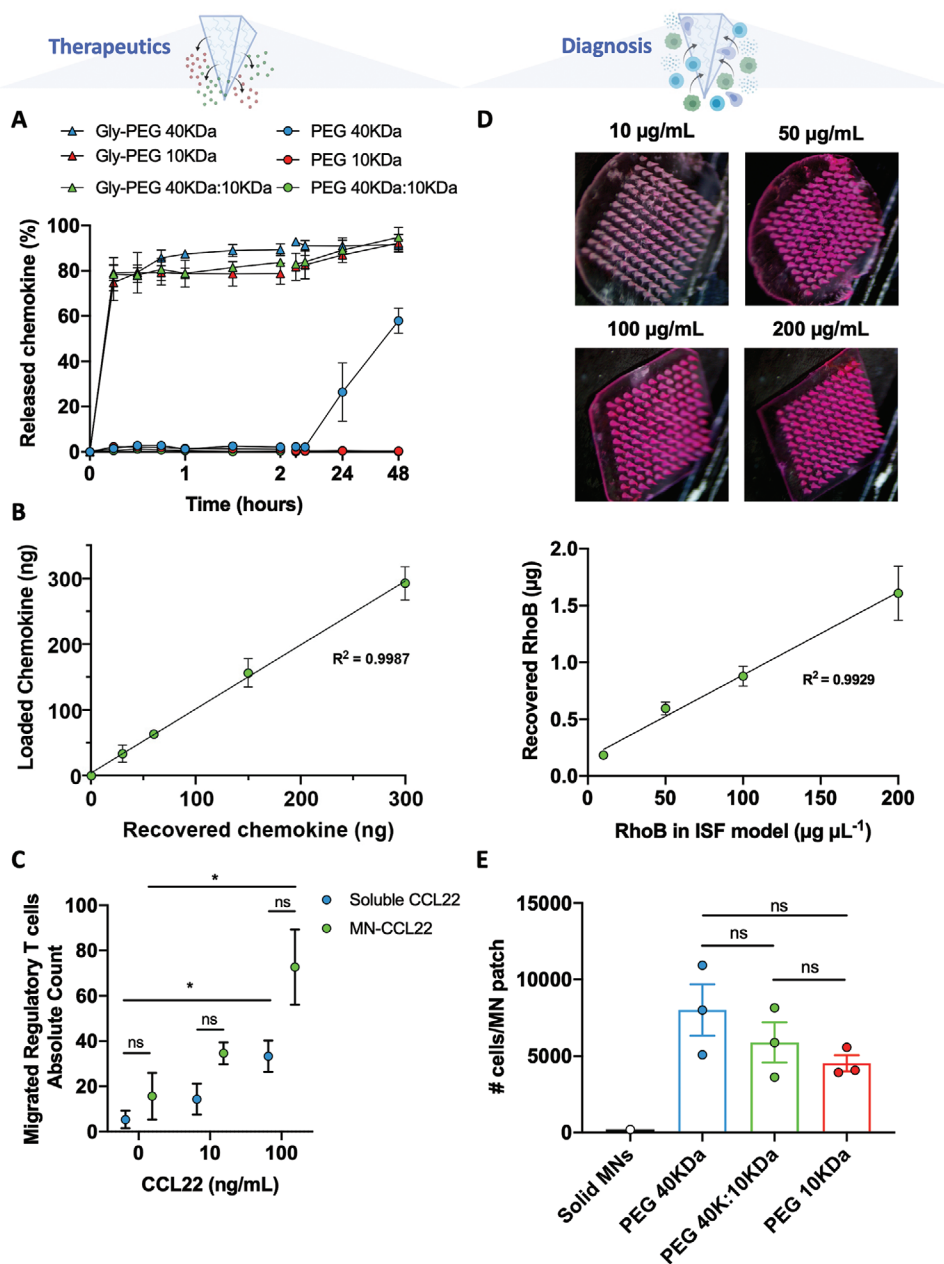


Figure 3. Characterization of MN-based platform for chemokine delivery and immune cell sampling in vitro. A) Release of IL-2 from the HA-based hydrogels was quantified by tracking the fluorescence signal of the labeled IL-2 over time. B) Analysis of the MNs loading capacity by means of fluorescence quantification (plotted as initially loaded mass of IL-2 versus recovered mass of IL-2, $R^2 = 0.9987$). C) Comparison of T_{reg} migration as a function of CCL22 concentration when soluble or MN-loaded D) Analyte recovery (RhoB) from mimetic skins with HA-derived MNs, $R^2 = 0.9929$. E) Recovered immune cells from digested HA-based MNs as quantified by flow cytometry. Data is represented as mean \pm s.d. ($n = 3$). Multiple comparisons among groups were determined using either one-way ANOVA followed by a post-hoc test or non-parametric t-test (Mann-Whitney) when applicable. P-value: ns = not significant, $*p < 0.05$, $**p < 0.01$.

on the mouse allografts, which reflect successful penetration of the MNs to the epidermis layer, and without causing any major injury or bleeding. Using quantitative PCR technique, we studied differential expression of CD3 as universal T cell marker (cell infiltrates inducing allograft rejection), FOXP3 as a transcription factor differentiating T_{regs} from conventional T cells (T_{regs} suppress rejection), and IL-6 as a major pro-inflammatory cytokine involved in promoting graft rejection, normal-

ized to the expression of the house keeping gene GAPDH. Ratio of fold change in FOXP3 to CD3 expression was then used as an indicator of the effect of the delivered therapy on T_{reg} recruitment and proliferation compared to no treatment (Figure 4B). Skin allografts treated with CCL22+10 ng IL-2 and CCL22+100 ng IL-2 showed significantly increased ratio of FOXP3 to CD3 compared to allografts treated with empty MNs, confirming the therapeutic merit of MNs to induce on-target

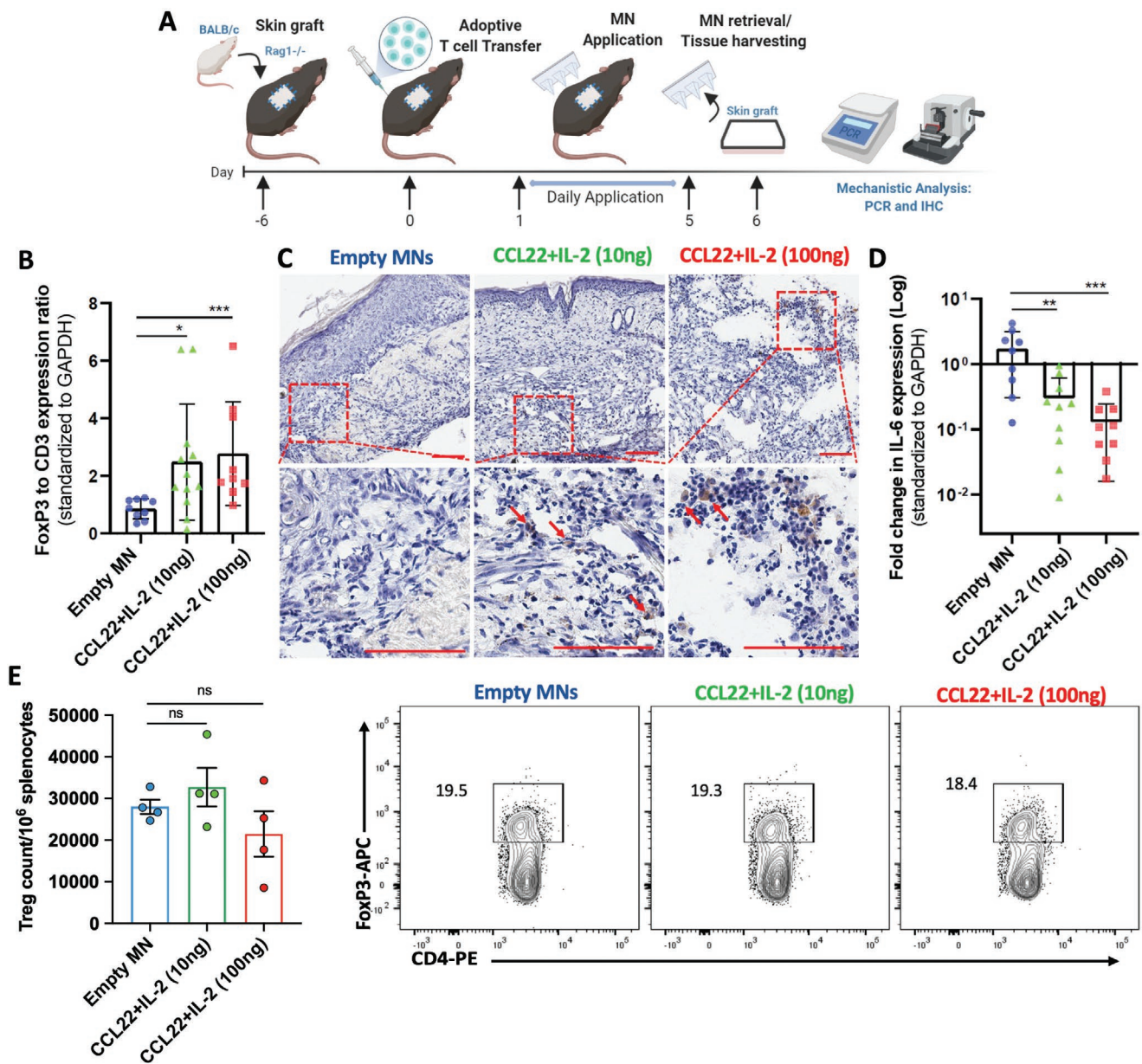


Figure 4. Delivery of HA-based MNs loaded with CCL22 and IL-2 to skin allografts results in increased T_{reg} recruitment. A) Study design of skin allograft transplant model. 10 mm x15 mm skin patch from BALB/c was transplanted onto the dorsal trunk of a $Rag1^{-/-}$ mouse on C57BL/6 background. On day 6 post-transplant, T lymphocytes were adoptively transferred and MNs were next applied consecutively for 5 days. On day 7 post adoptive transfer, allografts were harvested and analyzed by RT-PCR. ($n = 4$ to 6 biological replicates per condition, 2 separate experiments) B) Quantification of FOXP3 to CD3 gene expression by RT-PCR. C) Intra-graft T_{reg} proliferation was assessed by IHC using FOXP3 as T_{reg} differential biomarker. Scale bar = 100 μ m. D) Quantification of the fold change in IL-6 gene expression by RT-PCR. E) Quantification and representative flow-cytometry-dot-plot of the number of T_{regs} (FOXP3⁺; CD4⁺) per million of splenocytes. Multiple comparisons among groups were determined using either one-way ANOVA followed by a post-hoc or non-parametric t-test (Mann-Whitney) when applicable. P-value: ns = not significant, * $p < 0.05$, ** $p < 0.01$, *** $p < 0.001$

T_{reg} proliferation. Significant differences in T_{reg} proliferation among treatments were not observed. In agreement with RT-PCR analysis, intra-graft T_{reg} presence was demonstrated in those mice administered CCL22 and IL-2 using HA-derived MNs (Figure 4C). In contrast, infiltration of T_{regs} into skin allografts administered with empty MNs was not observed. Treatment of the allografts with combination of CCL22 and IL-2 resulted in significant reduction in IL-6 expression, with grafts treated with CCL22+100 ng IL-2 showing more than ten times

reduction in IL-6, indicating reduced inflammation at the allograft site (Figure 4D).

2.5. Delivery of CCL22 and IL-2 with MNs did not Induce T_{reg} Expansion in Peripheral Organs

To study the systemic effects of MN-mediated local delivery of IL-2, T_{reg} populations were evaluated in splenocytes harvested

from allograft recipients on day 7 post-adoptive transfer. Our data showed comparable T_{reg} numbers for all the groups and no significant T_{reg} expansion in the spleens (Figure 4E). In our previous work we found that systemic administration of IL-2 promoted T_{reg} proliferation in the spleen but failed to do so in the skin allografts, which aggravated their outcomes.^[51] Here, we confirmed minimal systemic effects following MN-based delivery of IL-2 suggesting the enhanced safety of our localized platform when compared to systemic routes and the potential to modulate immune cell composition and reduce inflammation locally.

2.6. Cells Captured by MNs can be Temporally Monitored Following Retrieval and Rapid MN Digestion

Next, we assessed the MNs potential in sampling cells from the skin allograft tissue to report on transplant state following therapy. We applied the MNs and retrieved them from the skin after 24 h of application. MNs were then digested with 10 mM TCEP, centrifuged and resuspended in full media, and stained with fluorochrome-labeled antibodies for flow cytometry phenotyping (Figure 5A). Indeed, MNs that delivered CCL22 and IL-2 had a higher number of T_{regs} entrapped in them compared to empty needles (Figure 5B). To validate that this reflected the immune state in the skin allograft, the presence of T_{regs} in the

allograft skin biopsy was tested by flow cytometry. Flow cytometry plots corroborated the presence of higher percentage of T_{regs} in the skin allograft treated with CCL22+ IL-2 (10 ng) MNs compared to Empty MN controls, in agreement with the T_{reg} distribution observed from retrieved ISF following microneedle sampling (Figure 5C).

3. Conclusion

We have synthesized a new HA-based MN, allowing for rapid chemokines release and skin ISF extraction, to recruit and sample T_{regs} . Our MN platform is composed of amine-modified HA hydrogel crosslinked with 8-arm-PEG-NHS, providing with high swelling capacity to afford drug release and enhanced cell infiltration. In addition, the presence of disulfide bonds in the amine-modified HA structure allows for its degradation—in less than 5 min—for subsequent analysis of immune cells. In vivo studies confirmed that CCL22 and IL-2 loaded HA-based MNs induce T_{reg} recruitment and expansion in the skin transplant site without inducing significant systemic effects. Moreover, the HA-based MN platform allowed for sampling of the T_{reg} homing process, which opens up numerous potential avenues for the early detection of rejection episodes, increasing the prospects of graft survival.

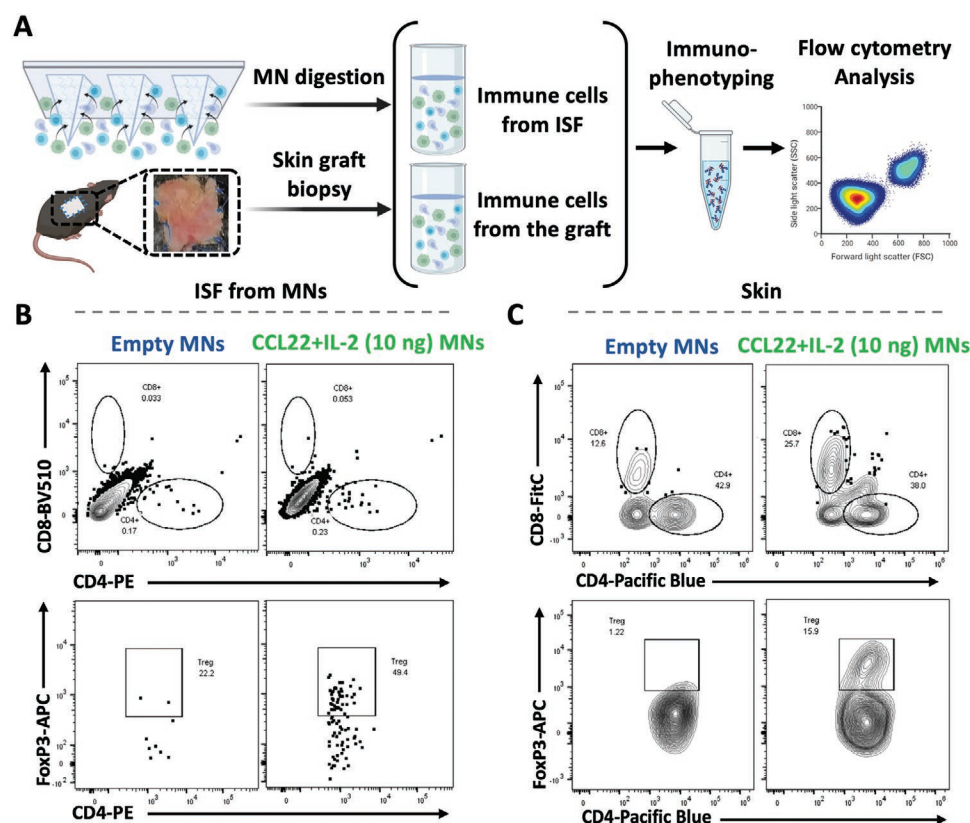


Figure 5. Monitoring the T_{reg} homing process using HA-based MNs. A) Scheme of immune cell sampling using HA-based MNs or whole allograft biopsy. On day 7 post adoptive T cell transfer, MNs were harvested along with skin allografts ($n = 4$ to 6 biological replicates per condition, 2 separate experiments). MNs were digested under reducing conditions and allografts enzymatically. Cells were next stained and analyzed by flow cytometry. CD8⁺, CD4⁺, and FOXP3⁺ representative flow cytometry dot plots from B) retrieved ISF and C) skin allografts.

4. Experimental Section

Materials: All reagents and solvents were purchased from Sigma Aldrich unless otherwise stated. Sodium hyaluronate (60 kDa) was obtained from LifeCore Medical with a purity of at least 95%. NHS-terminated 8-arm PEG was purchased from Creative PEG Works. MN PDMS custom-made molds (11 × 11 needles with height 600 μm, base width 300 μm and tip to tip spacing of 600 μm) were obtained from Blueacre Technology. CCL22 and IL-2 chemokines were purchased from Peptidech.

Synthesis of Amino-Modified Hyaluronic Acid (HA-SS-NH₂)
Polymer: 60 kDa-sodium hyaluronate (1% w/v in MES buffer) was activated with N-(3-(dimethylamino)propyl)carbodiimide (EDC) and N-hydroxysuccinimide (NHS) at a 1:4:2 molar ratio and reacted at room temperature for 30 min. The activated HA was then mixed with Cysteamine Dihydrochloride at 1:10 molar ratio and reacted at room temperature for 12 h. HA-SS-NH₂ was purified by dialysis against deionized water for 6 days at room temperature, freeze dried, and stored at -20 °C protected from humidity until use. For structural analysis, modified HA-SS-NH₂ was dissolved in D₂O and analyzed by ¹H-NMR, recorded using a 400 MHz Varian NMR spectrometer (NMR Instruments, Clarendon Hills, IL).

Fluorescent Labeling of HA-SS-NH₂ Polymer: HA-SS-NH₂ polymer was fluorescently tagged with AlexaFluor 647 carboxylic acid succinimidyl ester (AF647) at 1:0.1 molar ratio (HA-SS-NH₂: AF647). HA-SS-NH₂ polymer in 0.1 M bicarbonate buffer (pH 8.5) was mixed with AF647 and reacted for 1 h at room temperature in the dark. HA-SS-NH₂-AF647 polymer was washed with PBS and recovered by centrifugal filtration (10 kDa MWCO, Millipore) at 14 000 rpm for 15 min at 4 °C.

HA Hydrogel Disks Fabrication: 100 μL of hydrogel disks for streamlined screening were prepared by mixing equal volumes of HA-SS-NH₂ polymer (10% w/v) and the 8-arm-PEG-NHS crosslinker (10% w/v). Solutions were dissolved separately with phosphate buffer (pH = 7.4) and vigorously mixed together for 10 s inside cylindrical plastic molds (diameter: 5.00 mm; height: 2.50 mm). Hydrogel disks were allowed to react for 5 min to ensure full gelation, freeze-dried, and stored at room temperature protected from humidity until use.

HA-Based MN Fabrication: MNs were produced using custom-made molds consisting of an 11 × 11 array of negative MNs projections, each one with a height of 600 μm and a radius of 150 μm. First, HA-SS-NH₂ polymer (10% w/v in phosphate buffer, pH = 7.4) was cast on top of the molds and centrifuged at 4200 rpm for 5 min. Excess polymer was removed, and molds were freeze-dried. Then, 8-arm-PEG-NHS crosslinker (10% w/v in phosphate buffer, pH = 7.4) was cast and forced by centrifugation through the mold under the same conditions. This approach, together with the gradual gelation of hydrogel, ensured a successful polymerization of the matrix from “tip-to-tip” of the MNs and a homogenous composition. Excess polymer was carefully removed, and molds were freeze-dried. Next, an aqueous solution containing chemokines and glycine (10 ng mL⁻¹) was deposited and briefly spined for 15 s. Immediately after, a polymeric backing layer of PLGA (Resomer RG 858 S, Sigma-Aldrich, USA) at 15% (w/v) dissolved in acetonitrile was added dropwise until covering the whole area of the mold. Finally, HA-based MNs were allowed to dry at room temperature for 12 h, peeled off the molds carefully, and stored at room temperature preserved from humidity.

Swelling Studies with HA-Based Hydrogel Disks: HA-based hydrogels disks were incubated with PBS at 37 °C and their weight was recorded over time (W_i) and normalized to their respective dry weight (W_0). Swelling percentage was assessed as a function of mass increase over time and calculated as: $W_i \times 100/W_0$.

Skin Penetration Studies: Penetration capacity of the HA-based MNs was tested ex vivo and in vivo in shaved C57BL/6 and in Rag1^{-/-} mice with skin allografts. HA-based MNs were applied and kept in place using medical-grade tape (FLEXcon, USA) for 1 h. Skin penetration was confirmed by surface staining with blue Shandon Tissue-Marking Dye (ThermoFisher) and further imaged by optical microscopy.

On-Demand Digestion of HA-Derived Hydrogel Matrices: HA-based MNs or HA-based hydrogels were incubated with 10 mM Tris (2-carboxyethyl) phosphine (TCEP) solution in supplemented cell culture media or PBS at pH 7.4 (depending on whether cells were collected). HA-based MNs or HA-based hydrogels were incubated under rotation at 37 °C for 10 min and the recovered suspension was filtered with a 70 μm cell strainer (BD bioscience) to remove any impurities.

Cell Lines: Human monocyte THP-1 cells (ATCC) were maintained in RPMI 1640 supplemented with 10% FBS, 2 mM L-glutamine, 25 mM HEPES, 100 μg mL⁻¹ Normocin (InvivoGen), and 100 U mL⁻¹ penicillin and 100 μg mL⁻¹ streptomycin. Cell lines were maintained in a humidified incubator at 37 °C and 5% CO₂.

Cytotoxicity Studies: THP-1 cells were incubated with different concentrations of digestion media (TCEP solution in supplemented media), ranging from 0.1 to 100 mM, for 10 min. Thereafter, digestion media was removed, and cells were stained using the LIVE/DEAD fixable Violet Dead Cell Stain Kit (ThermoFisher Scientific, USA) following the manufacturer's guidelines. Dead cells were analyzed by flow cytometry using a BD LSRFortessa flow cytometer.

Study of Chemokine Release Kinetics: Recombinant human IL-2 was fluorescently labeled with the Lightning-Link Rapid Alexa Fluor594 kit (Novus Biologicals, USA) following the manufacturer's instructions. Release studies were conducted with HA-based MNs loaded with labeled IL-2. IL-2 loaded HA-based MNs were placed in Eppendorf tubes, immersed with PBS (1 mL), and incubated under rotation at 37 °C. 100 μL of PBS was replaced at a predetermined time point, and IL-2 fluorescence was assessed by checking the fluorescence at 650–665 nm using a Microplate Reader.

HA-Based MNs Loading Capacity: HA-based MNs were loaded with labeled IL-2 concentrations. IL-2 loaded MNs were digested as previously described and IL-2 loading capacity was assessed by checking the IL-2 fluorescence at 650–665 nm using a Microplate Reader.

Analysis of Chemokine Stability by ELISA: HA-derived MNs loaded with 100 ng of CCL22 were fabricated and stored for 2, 15, or 30 days at 1) room temperature, 2) 4 °C, or 3) -80 °C protected from humidity. Next, MNs were digested under reducing conditions using TCEP (10 mM) and supernatants were analyzed by Cytokine ELISA using the R&D Mouse CCL22/MDC Quantikine ELISA Kit following the manufacturer's guidelines.

Recovery of Immune Cells from HA-Based MNs: HA-based MN patches were incubated with 1×10^6 THP-1 cells per well for 24 h. Then, MNs were washed with PBS to minimize unspecific interactions between cells and the MN backing layer and digested as previously described. After digestion, cells were pelleted and stained with the CellTrace CFSE Cell Proliferation Kit Protocol (ThermoFisher Scientific, USA) following the manufacturer's instructions. Total number of infiltrated cells was quantified by flow cytometry using a BD LSR II.

Recovery of Soluble Analytes in a Mimetic Skin Model: Analyte recovery capacity of hydrogel-based MNs was conducted as detailed elsewhere using a skin model attempting to mimic the mechanical properties of the epidermis/ISF interface.^[40,41] 1.4% w/v agarose hydrogels containing increasing amounts of the model metabolite Rhodamine B were polymerized in 30 mm × 15 mm petri dishes and covered and with a stretched layer of parafilm aiming to emulate the properties of the water-impermeable stratum corneum. MN patches were left inserted in the agarose gels for two hours to reach a swelling plateau and subsequently digested as previously described. Finally, absorbance of the recovered analytes was measured in a plate reader ($\lambda = 553$ nm) and correlated with the extracted mass.

Animal Experiments: C57BL/6j (B6 wild type; #000 664), BALB/cj (BALB/c wild type; #000 651), and B6.129S7-Rag1tm1Mom (B6 Rag1^{-/-}, #002 216) mice were purchased from The Jackson Laboratory (Bar Harbour, ME, USA) and housed under specific-pathogen-free conditions at the Brigham and Women's Hospital animal facility. All mouse work was performed in compliance with ethical regulations and was approved by the Institutional Animal Care and Use Committee of Brigham and Women's Hospital. Age and sex-matched mice (6–8 weeks,

male and female) were randomized into experimental and control groups for all experiments.

Murine Skin Transplantation: A fully MHC-mismatched murine skin transplant model was successfully used as previously described.^[51] Briefly, full-thickness trunk skin grafts (1.0 cm by 1.5 cm) from BALB/c donors were harvested and connective, adipose, and panniculus carnosus tissues were cleared using blunt-tipped forceps. The fur of each anesthetized recipient Rag1^{-/-} mouse was shaven at the dorsal trunk, 1.0 cm by 1.5 cm of the recipient mouse's skin was excised, and an equally sized skin graft was sutured onto the graft bed with 6-0 prolene suture (Ethicon, #8695G). Skin transplants were secured with dry gauze and bandaged for 7 days before adoptive cell transfer and MN application

Analysis of Immune Infiltrate by Flow Cytometry: A single cell suspension of skin grafts was obtained as previously described.^[51] In brief, skin grafts were harvested, minced into 0.5 mm fragments, and digested in a solution of RPMI supplemented with 10% Fetal Bovine Serum, 1% Penicillin and Streptomycin (100 IU mL⁻¹ Penn, 100 µg mL⁻¹ Strep), and collagenase P (stock concentration 1 mg mL⁻¹; Cat no: 11 213 865 001, Roche) for 3 h at 37 °C. Afterwards, skin grafts were re-incubated for 15 min at room temperature after adding 200 Kunitz Units mL⁻¹ of recombinant DNase I (Cat no: 10 104 159 001, Roche) to reduce DNA fragments and clumping. The solution was then filtered through 70 µm mesh filters and centrifuged at 800 g for 8 min, then resuspended in Full media supplemented with 20% FBS and incubated at 37 °C overnight to recover from enzymatic treatment. Then cells were resuspended in FACS staining buffer (1× DPBS, 1.0% Bovine Serum Albumin, 0.02% sodium azide (Sigma-Aldrich)) for flow cytometry analysis. Cells were counted manually using a hemocytometer and stained with fluorescent antibodies at a maximum concentration of 1 × 10⁶ cells in 100 µL FACS staining buffer (BioLegend). The following anti-mouse antibodies were purchased from eBioscience: CD45 PE-Cy7 (clone 30-F11), FOXP3 APC (clone FJK-16S), CD4 PE (clone RM4-5), and BD Biosciences: CD3 PerCP Cy5.5 (clone 500A2), CD8 Alexa Flour 488 (clone 53-6.7). Dead cells were stained using Fixed Viability Dye eFluor780 (eBioscience). Stained cells were analyzed by flow cytometry using a BD FACS Canto II cytometer (BD Biosciences) and all data were analyzed using FlowJo version 10 (FlowJo LLC).

CCL22- Dependent Trans-Well Migration Assay: Recruitment of T_{regs} as a function of CCL22 was assessed in a 24-well plate containing a 5 µm-pore polycarbonate transwell filter system (Costar transwell permeable support #3421). MNs loaded with incremental amounts of CCL22 (0, 10, and 100 ng) or equivalent dose of soluble CCL22 were added in the receiver wells and incubated at 37 °C for 1 h. 5 × 10⁵ CD3⁺ T cells were magnetically isolated from C57BL/6 mice using mouse T cell isolation kit (EasySep, # 19 851) and resuspended in full culture media and added to the top wells. Cells were then incubated at 37 °C and 5% CO₂ for 3 h. Cells in the receiver well were then harvested and stained with Fixed viability dye, anti-CD3, CD4, CD25, and FOXP3 antibodies and analyzed by flow cytometry.

Quantitative Real-Time Polymerase Chain Reaction: Quantitative real-time polymerase chain reaction (qPCR) was used to assess the differential expression of mRNA transcripts between control (Empty MN) and CCL22+ IL-2 (10 or 100 ng) groups. A small piece of each allograft was kept in RNAprotect tissue reagent (Qiagen, Cat. #76 104) on the same day skin allografts were harvested for digestion and flow cytometry analysis. Later, the skin grafts were partially thawed and 1 mm² pieces were cut to finer pieces. RNA was then isolated using RNA isolation kit (Qiagen RNeasy plus Mini Kit, Cat.# 4136) following the manufacturer's protocol. Eluted RNA concentration was measured. The RNA concentration was measured with a NanoDrop 2000 Spectrophotometer (ThermoFisher Scientific, Waltham, MA, United States) and complementary DNA strands were reverse transcribed with iScript Reverse Transcription Supermix (#1 708 841, Bio-Rad Laboratories) as per the manufacturer's protocol and the product was stored at -20 °C till further use. Quantitative real-time PCR was performed in 0.1 mL MicroAmp Fast Optical 96-Well Reaction Plates

(Applied Biosystems, #4 346 906) with 30 ng of ds-RNA per mRNA target, 500 nm forward and 500 nm reverse primers, and SsoAdvanced Universal SYBR Green Supermix (#1 725 274, Bio-Rad Laboratories) diluted to 1× with PCR-grade water (#W4502, Sigma-Aldrich) in 10-µL reaction volumes. Primer pairs were based on OriGene's qSTAR qPCR Primer Pairs (Rockville, MD, United States) and synthesized through Integrated DNA Technologies (Coralville, IA, United States). Cycle threshold (Ct) values were measured with QuantStudio 3 (ThermoFisher Scientific, Waltham, MA, United States). Ct values were then corrected with GAPDH housekeeping gene expression per replicate, per run, log₂ normalized, averaged for the control replicates, and deviation from the average was calculated per condition, per replicate. Fold change of FOXP3 to CD3 was calculated by dividing fold change of FOXP3 to fold change of CD3 (each separately normalized to GAPDH) and fold change of IL-6 was presented after normalization to GAPDH.

Analysis of Intra-graft T_{reg} Proliferation by Immunohistochemistry: Skin tissue sections were processed and imaged by the Hope Babette Tang Histology facility at the Koch Institute of Integrative Cancer Research at MIT (Cambridge, USA). Briefly, 0.5 cm² allograft sections harvested on the day of mechanistic analysis were embedded in OCT. Samples were flash-frozen in a bath of dry ice and preserved at -80 °C until sectioning. Allografts were cryosectioned into 5 µm-wide tissue sections and FOXP3 expression was confirmed via indirect staining using HRP-conjugated antibodies and visualized using DAB substrate. Slides were counterstained with Hematoxylin (coloring nuclei in blue) to help orient with respect to the FOXP3 staining. Processing of the microscopic images was performed using the Aperio ImageScope 12.3.3 software (Leica).

Analysis of the Mechanical Strength of the HA-Derived MNs: Mechanical properties of the MNs when empty or chemokine-loaded were measured using a micro-force test station with a mechanical sensor (3400 Series, Instron, USA). Briefly, MN patches were placed on the surface of the platform with the needle-like projections facing up. Then, the MN patch was compressed by the moving sensors at a constant rate of 0.6 mm min⁻¹. The displacement and force applied on the MNs were recorded from the moment the sensors touched the uppermost tip of the MNs until a maximum force of ≈100 N was reached. After the test, the force-travel curves of MNs arrays were obtained accordingly by correlating the compressive strain or displacement (%) with the compressive stress (kPa). Finally, the Young's modulus or modulus of elasticity in tension was calculated from the slope in the elastic (or linear) portion of the physical stress-strain curve (GPa).

Statistical Analysis: Statistical analyses were carried out using Graph-Pad Prism 8 (GraphPad Software). For in vitro experiments, a minimum of n = 3 biological replicates were used per condition in each experiment. Pairwise comparisons were performed using Student t-tests. Multiple comparisons among groups were determined using one-way ANOVA followed by a post-hoc test. For in vivo experiments, a minimum of n = 4 biological replicates were used per condition in each experiment. Multiple comparisons among groups were determined using non-parametric t-test (Mann-Whitney). No specific pre-processing of data was performed prior to statistical analyses. Differences between groups were considered significant at p-values below 0.05 (*p < 0.05, **p < 0.01, ***p < 0.001).

Supporting Information

Supporting Information is available from the Wiley Online Library or from the author.

Acknowledgements

N.P., P.D., Z.S., and K.Y. contributed equally to this work. N.A. and J.A. thank the Department of Medicine at Brigham and Women's Hospital for the Innovation Evergreen Fund (IEF) Award that supported our work.

Conflict of Interest

The authors declare no conflict of interest.

Data Availability Statement

The data that support the findings of this study are available on request from the corresponding author. The data are not publicly available due to privacy or ethical restrictions.

Keywords

diagnosis, immune regulation, local delivery, microneedles, skin transplants, therapy

Received: January 5, 2021

Revised: April 26, 2021

Published online: May 24, 2021

- [1] A. V. Nguyen, A. M. Soulika, *Int. J. Mol. Sci.* **2019**, *20*, 1811.
- [2] S. Sakaguchi, T. Yamaguchi, T. Nomura, M. Ono, *Cell* **2008**, *133*, 775.
- [3] L. A. Kalekar, M. D. Rosenblum, *Int. Immunol.* **2019**, *31*, 457.
- [4] S. M. Kang, Q. Tang, J. A. Bluestone, *Am. J. Transplant.* **2007**, *7*, 1457.
- [5] M. J. Wolff, J. M. Leung, M. Davenport, M. A. Poles, I. Cho, P. Loke, *PLoS One* **2012**, *7*, e41373.
- [6] N. Ali, M. D. Rosenblum, *Immunology* **2017**, *152*, 372.
- [7] T. Hartwig, P. Zwicky, B. Schreiner, N. Yawalkar, P. Cheng, A. Navarini, R. Dummer, L. Flatz, C. Conrad, C. Schlapbach, B. Becher, *Cell Rep.* **2018**, *25*, 3564.
- [8] R. M. Trüeb, M. F. R. G. Dias, *Clin. Rev. Allergy Immunol.* **2018**, *54*, 68.
- [9] E. Castela, F. Le Duff, C. Butori, M. Ticchioni, P. Hofman, P. Bahadoran, J. P. Lacour, T. Passeron, *JAMA Dermatol.* **2014**, *150*, 748.
- [10] J. D. Turissini, T. Elmarsafi, K. K. Evans, P. J. Kim, *Georg. Med. Rev.* **2019**, *3*, 1.
- [11] M. Uehara, X. Li, A. Sheikhi, N. Zandi, B. Walker, B. Saleh, N. Banouni, L. Jiang, F. Ordikhani, L. Dai, M. Yonar, I. Vohra, V. Kasinath, D. P. Orgill, A. Khademhosseini, N. Annabi, R. Abdi, *Sci. Rep.* **2019**, *9*, 6535.
- [12] E. Rezaei, A. Beiraghi-Toosi, A. Ahmadabadi, S. H. Tavousi, A. A. Tabrizi, K. Fotuhi, M. J. Nooghabi, A. Manafi, S. A. Moghadam, *World J. Plast. Surg.* **2017**, *6*, 94.
- [13] A. Klimczak, M. Siemionow, *Semin. Plast. Surg.* **2007**, *21*, 226.
- [14] Q. Tang, J. A. Bluestone, *Cold Spring Harb. Perspect.* **2013**, *3*, a015552.
- [15] J. Zhou, W. He, G. Luo, J. Wu, *Arch. Immunol. Ther. Exp.* **2013**, *61*, 397.
- [16] K. J. Wood, A. Bushell, J. Hester, *Nat. Rev. Immunol.* **2012**, *12*, 417.
- [17] C. I. Kingsley, M. Karim, A. R. Bushell, K. J. Wood, *J. Immunol.* **2002**, *168*, 1080.
- [18] X. X. Zheng, A. Sánchez-Fueyo, M. Sho, C. Domenig, M. H. Sayegh, T. B. Strom, *Immunity* **2003**, *19*, 503.
- [19] G. Camirand, L. V. Riella, *Am. J. Transplant.* **2017**, *17*, 601.
- [20] R. Setoguchi, S. Hori, T. Takahashi, S. Sakaguchi, *J. Exp. Med.* **2005**, *201*, 723.
- [21] O. Boyman, M. Kovar, M. P. Rubinstein, C. D. Surh, J. Sprent, *Science* **2006**, *311*, 1924.
- [22] C. G. Brunstein, B. R. Blazar, J. S. Miller, Q. Cao, K. L. Hippen, D. H. McKenna, J. Curtsinger, P. B. McClave, J. E. Wagner, *Biol. Blood Marrow Transplant.* **2013**, *19*, 1271.
- [23] R. Baluna, E. S. Vitetta, *Immunopharmacology* **1997**, *37*, 117.
- [24] M. Hirakawa, T. Matos, H. Liu, J. Koreth, H. T. Kim, N. E. Paul, K. Murase, J. Whangbo, A. C. Alho, S. Nikiforow, C. Cutler, V. T. Ho, P. Armand, E. P. Alyea, J. H. Antin, B. R. Blazar, J. F. Lacerda, R. J. Soiffer, J. Ritz, *JCI Insight* **2016**, *1*, e89278.
- [25] Y. Grinberg-bleyer, A. Baeyens, S. You, R. Elhage, G. Fourcade, S. Gregoire, N. Cagnard, W. Carpentier, Q. Tang, J. Bluestone, L. Chatenoud, D. Klatzmann, B. L. Salomon, E. Piaggio, *J. Exp. Med.* **2010**, *207*, 1871.
- [26] B. D. Sather, P. Treuting, N. Perdue, M. Miazgowiec, J. D. Fontenot, A. Y. Rudensky, D. J. Campbell, *J. Exp. Med.* **2007**, *204*, 1335.
- [27] J. Montane, M. Obach, S. Alvarez, L. Bischoff, D. L. Dai, G. Soukhatcheva, J. J. Priatel, G. Hardenberg, M. K. Levings, R. Tan, P. C. Orban, C. B. Verchere, *Cell Transplant.* **2015**, *24*, 2143.
- [28] J. Montane, L. Bischoff, G. Soukhatcheva, D. L. Dai, G. Hardenberg, M. K. Levings, P. C. Orban, T. J. Kieffer, R. Tan, C. B. Verchere, *J. Clin. Invest.* **2011**, *121*, 3024.
- [29] J. D. Fisher, W. Zhang, S. C. Balmert, A. M. Aral, A. P. Acharya, Y. Kulahci, J. Li, H. R. Turnquist, A. W. Thomson, M. G. Solari, V. S. Gorantla, S. R. Little, *Sci. Adv.* **2020**, *6*, eaax8429.
- [30] S. Jhunjhunwala, G. Raimondi, A. J. Glowacki, S. J. Hall, D. Maskarinec, S. H. Thorne, A. W. Thomson, S. R. Little, *Adv. Mater.* **2012**, *24*, 4735.
- [31] O. Joffre, T. Santolaria, D. Calise, T. Al Saati, D. Hudrisier, P. Romagnoli, J. P. M. Van Meerwijk, *Nat. Med.* **2008**, *14*, 88.
- [32] E. Ingulli, *Pediatr. Nephrol.* **2010**, *25*, 61.
- [33] Y. Ye, J. Yu, D. Wen, A. R. Kahkoska, Z. Gu, *Adv. Drug Deliv. Rev.* **2018**, *127*, 106.
- [34] Y.-C. Kim, J. H. Park, M. R. Prausnitz, *Adv. Drug Delivery Rev.* **2012**, *64*, 1547.
- [35] D. Church, S. Elsayed, O. Reid, B. Winston, R. Lindsay, *Clin. Microbiol. Rev.* **2006**, *19*, 403.
- [36] X. Zhang, G. Chen, F. Bian, L. Cai, Y. Zhao, *Adv. Mater.* **2019**, *31*, 1.
- [37] P. P. Samant, M. M. Niedzwiecki, N. Raviele, V. Tran, J. Mena-lapaix, D. I. Walker, E. I. Felner, D. P. Jones, G. W. Miller, M. R. Prausnitz, *Sci. Transl. Med.* **2020**, *12*, eaaw0285.
- [38] D. Al Sulaiman, J. Y. H. Chang, N. R. Bennett, H. Topouzi, C. A. Higgins, D. J. Irvine, S. Ladame, *ACS Nano* **2019**, *13*, 9620.
- [39] M. Zheng, Z. Wang, H. Chang, L. Wang, S. W. T. Chew, D. Chin, S. Lio, M. Cui, L. Liu, B. C. K. Tee, C. Xu, *Adv. Healthcare Mater.* **2020**, *9*, 1901683.
- [40] H. Chang, M. Zheng, X. Yu, A. Than, R. Z. Seeni, R. Kang, J. Tian, D. P. Khanh, L. Liu, P. Chen, C. Xu, *Adv. Mater.* **2017**, *29*, 1702243.
- [41] R. He, Y. Niu, Z. Li, A. Li, H. Yang, F. Xu, F. Li, *Adv. Healthcare Mater.* **2020**, *9*, 1901201.
- [42] A. Mandal, A. V. Boopathy, L. K. W. Lam, K. D. Moynihan, M. E. Welch, N. R. Bennett, M. E. Turvey, N. Thai, V. H. Jenny, J. C. Love, P. T. Hammond, D. J. Irvine, *Sci. Transl. Med.* **2018**, *10*, eaar2227.
- [43] J. Pan, W. Ruan, M. Qin, Y. Long, T. Wan, K. Yu, Y. Zhai, *Sci. Rep.* **2018**, *8*, 1117.
- [44] P. Mikolajewska, R. F. Donnelly, M. J. Garland, D. I. J. Morrow, T. R. R. Singh, V. Iani, J. Moan, A. Juzeniene, *Pharm. Res.* **2010**, *27*, 2213.
- [45] H. Du, P. Liu, J. Zhu, J. Lan, Y. Li, L. Zhang, J. Zhu, J. Tao, *ACS Appl. Mater. Interfaces* **2019**, *11*, 43588.
- [46] E. Larrañeta, M. Henry, N. J. Irwin, J. Trotter, A. A. Perminova, R. F. Donnelly, *Carbohydr. Polym.* **2018**, *181*, 1194.
- [47] J. Zhu, X. Zhou, H. J. Kim, M. Qu, X. Jiang, K. J. Lee, L. Ren, Q. Wu, C. Wang, X. Zhu, P. Tebon, S. Zhang, J. Lee, N. Ashammakhi, S. Ahadian, M. R. Dokmeci, Z. Gu, W. Sun, A. Khademhosseini, *Small* **2020**, *16*, 1905910.

- [48] R. R. Misra, H. Suniti, M. Vincent, S. Ghatak, *Front. Immunol.* **2015**, *6*, 201.
- [49] D. J. Cline, S. E. Redding, S. G. Brohawn, J. N. Psathas, J. P. Schneider, C. Thorpe, *Biochemistry* **2004**, *43*, 15195.
- [50] P. Dosta, S. Ferber, Y. Zhang, K. Wang, A. Ros, N. Uth, Y. Levinson, E. Abraham, N. Artzi, *J. Biomed. Mater. Res.* **2020**, *7*, 2937.
- [51] S. K. Eskandari, I. Sulkaj, M. B. Melo, N. Li, H. Allos, J. B. Alhaddad, B. Kollar, T. J. Borges, A. S. Eskandari, M. A. Zinter, S. Cai, J. P. Assaker, J. Y. Choi, B. S. Al Dulaijan, A. Mansouri, Y. Haik, B. A. Tannous, W. J. Van Son, H. G. D. Leuvenink, B. Pomahac, L. V. Riella, L. Tang, M. A. J. Seelen, D. J. Irvine, J. R. Azzi, *Sci. Transl. Med.* **2020**, *12*, 1.